nature materials

SUPPLEMENTARY INFORMATION

https://doi.org/10.1038/s41563-020-0677-9

In the format provided by the authors and unedited.

Mechanism of collective interstitial ordering in Fe–C alloys

Xie Zhang[1,2]✉, Hongcai Wang[3]✉, Tilmann Hickel[2], Jutta Rogal[4], Yujiao Li[5] and Jörg Neugebauer[2]

[1]Materials Department, University of California, Santa Barbara, CA, USA. [2]Max-Planck-Institut für Eisenforschung GmbH, Düsseldorf, Germany. [3]Institut für Werkstoffe, Ruhr-Universität Bochum, Bochum, Germany. [4]Interdisciplinary Centre for Advanced Materials Simulation, Ruhr-Universität Bochum, Bochum, Germany. [5]Center for Interface-Dominated High Performance Materials (ZGH), Ruhr-Universität Bochum, Bochum, Germany.
✉e-mail: xiezhang@ucsb.edu; hongcai.wang@rub.de

Supplementary Information for "Mechanism of collective interstitial ordering in Fe-C alloys"

Xie Zhang[1,2,*], Hongcai Wang[3,*], Tilmann Hickel[2],

Jutta Rogal[4], Yujiao Li[5], and Jörg Neugebauer[2]

[1] *Materials Department, University of California, Santa Barbara, CA, USA*

[2] *Max-Planck-Institut für Eisenforschung GmbH, Düsseldorf, Germany*

[3] *Institut für Werkstoffe, Ruhr-Universität Bochum, Bochum, Germany*

[4] *Interdisciplinary Centre for Advanced Materials Simulation, Ruhr-Universität Bochum, Bochum, Germany*

[5] *Center for Interface-Dominated High Performance Materials (ZGH), Ruhr-Universität Bochum, Bochum, Germany and*

* e-mail: xiezhang@ucsb.edu; e-mail: hongcai.wang@rub.de

Note 1. Analytical dynamical matrix and Kanzaki forces

Here we present the analytical formulas for computing the dynamical matrix and Kanzaki forces in reciprocal space. For body-centered cubic (bcc) Fe, the dynamical matrix can be derived analytically by considering the first- and second-nearest-neighbor interactions, namely [1]

$$\begin{aligned} D_{11}(\mathbf{q}) &= 4ac_{44}\left[1-\cos\frac{aq_x}{2}\cos\frac{aq_y}{2}\cos\frac{aq_z}{2}\right], \\ &+ a(c_{11}-c_{44})\left[1-\cos(aq_x)\right] \end{aligned} \tag{1}$$

$$D_{12}(\mathbf{q}) = 2a(c_{12}+c_{44})\sin\frac{aq_x}{2}\sin\frac{aq_y}{2}\cos\frac{aq_z}{2}. \tag{2}$$

where a is the lattice constant of bcc Fe. c_{11}, c_{12} and c_{44} are the elastic constants of bcc Fe.

Regarding the Kanzaki forces, an analytical approach has also been developed [2]. Specifically, the concentration expansion coefficients are introduced as follows to describe the expansion produced by placing interstitial atoms at the O_x, O_y, and O_z octahedral interstices, respectively.

$$u_{ij}^0(1) = \begin{pmatrix} u_{33}^0 & 0 & 0 \\ 0 & u_{11}^0 & 0 \\ 0 & 0 & u_{11}^0 \end{pmatrix}, \tag{3}$$

$$u_{ij}^0(2) = \begin{pmatrix} u_{11}^0 & 0 & 0 \\ 0 & u_{33}^0 & 0 \\ 0 & 0 & u_{11}^0 \end{pmatrix}, \tag{4}$$

$$u_{ij}^0(3) = \begin{pmatrix} u_{11}^0 & 0 & 0 \\ 0 & u_{11}^0 & 0 \\ 0 & 0 & u_{33}^0 \end{pmatrix}. \tag{5}$$

Then, the Fourier components of the Kanzaki forces can be derived as

$$\begin{aligned} \mathbf{F}_3(\mathbf{q}) &= -\mathrm{i}a_0^2\exp(-\frac{1}{2}\mathrm{i}q_z a_0) \\ &(\sigma_{11}^0\sin\frac{q_x a_0}{2}\cos\frac{q_y a_0}{2}, \sigma_{11}^0\sin\frac{q_y a_0}{2}\cos\frac{q_x a_0}{2}, \sigma_{33}^0\sin\frac{q_z a_0}{2}) \end{aligned}. \tag{6}$$

where

$$\sigma_{11}^0 = (c_{11}+c_{12})u_{11}^0 + c_{12}u_{33}^0 \tag{7}$$

$$\sigma_{33}^0 = 2c_{12}u_{11}^0 + c_{11}u_{33}^0 \tag{8}$$

$$u_{11}^0 = \frac{da}{adn_3}, u_{33}^0 = \frac{dc}{adn_3} \tag{9}$$

Here a and c are the lattice constants, and n_3 is the probability of finding an interstitial atom in the O_z octahedral sublattice.

Similarly, $\mathbf{F}_1(\mathbf{q})$ and $\mathbf{F}_2(\mathbf{q})$ can be obtained by a cyclic permutation of the coordinate indices x, y, z and the index m. For instance, $\mathbf{F}_1(\mathbf{q})$ is given by the permutations $(m = 3) \rightarrow (m = 1)$, $x \rightarrow y$, $y \rightarrow z$, $z \rightarrow x$.

$$\begin{aligned}\mathbf{F}_1(\mathbf{q}) &= -\mathrm{i}a_0^2 \exp(-\frac{1}{2}\mathrm{i}q_x a_0) \\ &(\sigma_{33}^0 \sin\frac{q_x a_0}{2}, \sigma_{11}^0 \sin\frac{q_y a_0}{2}\cos\frac{q_z a_0}{2}, \sigma_{11}^0 \sin\frac{q_z a_0}{2}\cos\frac{q_y a_0}{2})\end{aligned}, \tag{10}$$

$$\begin{aligned}\mathbf{F}_2(\mathbf{q}) &= -\mathrm{i}a_0^2 \exp(-\frac{1}{2}\mathrm{i}q_y a_0) \\ &(\sigma_{11}^0 \sin\frac{q_x a_0}{2}\cos\frac{q_z a_0}{2}, \sigma_{33}^0 \sin\frac{q_y a_0}{2}, \sigma_{11}^0 \sin\frac{q_z a_0}{2}\cos\frac{q_x a_0}{2})\end{aligned}. \tag{11}$$

Notably, in Eqs. (6), (10) and (11), a consistent origin is used in the coordinate system. However, to use these equations in practice, one has to shift the origin to the location of the point defect (here C interstitial), such as (0.5, 0, 0), (0, 0.5, 0) or (0, 0, 0.5) for the three sublattices, respectively. Such a translational operation of the coordinates would lead to a cancelation of the exponential phase factors in the three equations, namely, $\exp(-\frac{1}{2}\mathrm{i}q_x a_0)$, $\exp(-\frac{1}{2}\mathrm{i}q_y a_0)$ and $\exp(-\frac{1}{2}\mathrm{i}q_z a_0)$. Hence, to use the analytical Kanzaki forces to calculate the strain induced interaction, one needs to remove the exponential phase factors in Eqs. (6), (10) and (11).

Note 2. Accuracy of the lattice Green's function

In this note, we inspect the accuracy of the lattice Green's function. Since the lattice Green's function is the inverse of the dynamical matrix, we compare the phonon dispersion of bcc Fe calculated from different approaches (analytical, finite displacement, and molecular dynamics) to experiment [3] in Fig. 1. The derivations of the analytical approach are provided in Note 1. The finite displacement approach is described in the Methods section of the manuscript. The technical details of the molecular dynamics approach can be found in Ref. [4]. Overall, the three approaches yield similar results and are all in good agreement with experiment, especially in the vicinity of Γ, which is the most important part for the present study. There is some discrepancy at the boundary of the Brillouin zone, e.g., the H point. This is because the analytical approach uses elastic constants as input and can well capture the long-wavelength limit, but overestimates the phonon frequencies at short-wavelength vectors. Due to error cancellation, the analytical results agree even better with experiment. However, the consistency between the results from the finite displacement method and molecular dynamics demonstrates that our calculated phonon frequencies (thus the lattice Green's function) are reliable, though the EAM potential [5] employed here is not perfectly accurate compared to experiment. Since our benchmarking result is from the same EAM potential, the choice of the potential seems appropriate. Therefore, the discrepancy in the long-range strain induced interaction does not stem from the lattice Green's function.

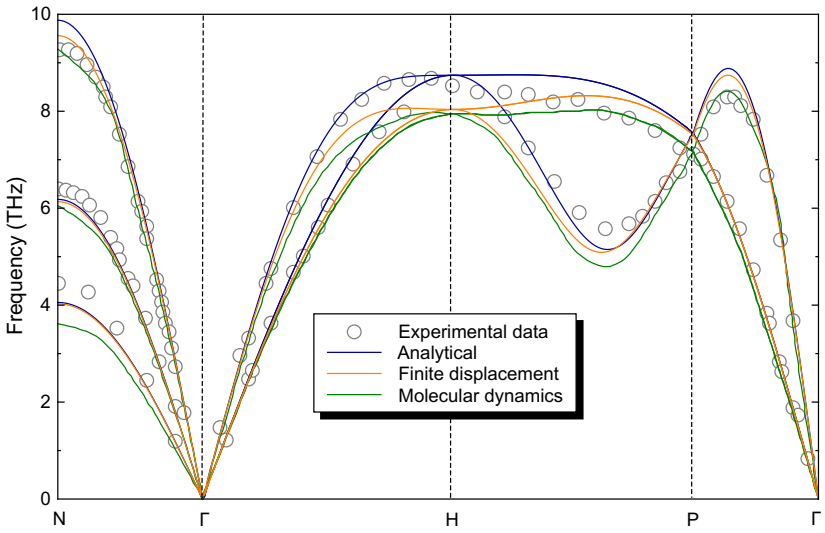

Fig. 1. Phonon dispersion of bcc Fe obtained from different approaches (analytical, finite displacement, and molecular dynamics). The experimental data are taken from Ref. [3].

Note 3. HRTEM characterization

Alloy ingots are produced by arc-melting electrolytic Fe (99.99 wt.% purity), Cr (99.99 wt.% purity), and a Fe-C pre-alloy (2.15 wt.% C) under vacuum. The ingots are flipped and melted 10 times during arc-melting to ensure homogeneity. The investigated microstructure was obtained by austenitizing the alloy at 1150 °C for four hours followed by quenching in water. Energy dispersive X-ray spectroscopy shows that Cr is homogeneously distributed in the lattice.

TEM thin foils are prepared by grinding 3 mm-diameter discs to a thickness of 50 μm, followed by twin-jet electropolishing in a TenuPol-5 (from Struers). Good thinning conditions are achieved using an electrolyte consisting of 70 vol.% methanol, 20 vol.% glycerin and 10 vol.% perchloric acid, flow rates between 15 and 20, and a voltage of 30 V at -11 °C. HRTEM imaging is performed at the rim of the electron transparent region, using an FEI Tecnai Supertwin F20 equipped with a field emission gun operating at 200 kV. The multi-slice method embedded within the Java electron microscopy simulation software (JEMS) is employed to simulate the HRTEM images using the atomic structures from EAM relaxations. A defocus of 75 nm with $C_s = 1.2$ mm is used. The specimen thickness is set to 35 nm as measured by the low-loss Electron Energy Loss Spectroscopy.

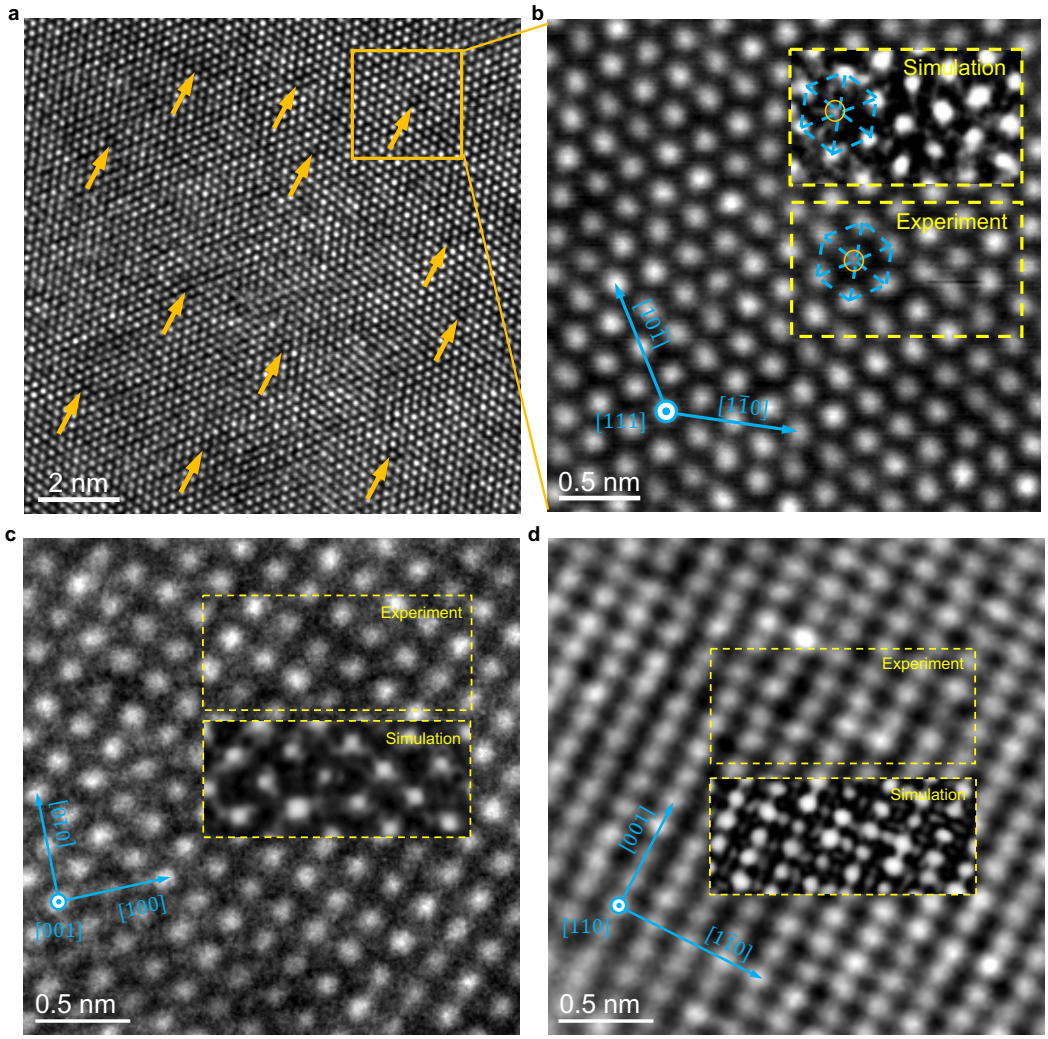

Fig. 2. **HRTEM analysis of the local strain fields induced by C interstitials. a**, HRTEM image of the $(111)_{\mathrm{bcc}}$ plane of a Fe-Cr-C alloy. Orange arrows highlight the "dark spots" associated with the local strain fields induced by C interstitials. **b**, An enlarged image of one local distortion field (orange box) in **a**. The two yellow dashed boxes show a comparison between the experimental HRTEM image and the one simulated using the distorted atomic structure from EAM relaxations. The orange circles and blue dashed lines depict the deviation of a Fe atom from its ideal lattice position (i.e., center of the hexagon). **c,d,** Similar analysis for the $(001)_{\mathrm{bcc}}$ and $(110)_{\mathrm{bcc}}$ planes of the Fe-Cr-C alloy, respectively.

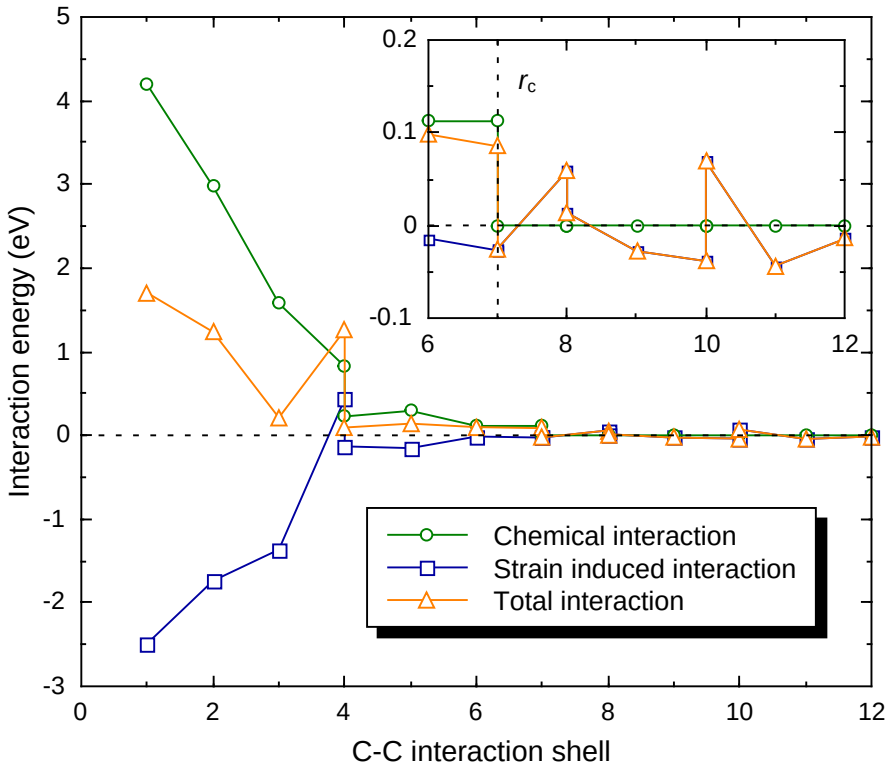

Fig. 3. **C-C interaction energies.** C-C interaction energies as a function of interaction shell computed directly from the EAM potential. The inset provides an enlarged view for the interactions at the $6^{\text{th}}-12^{\text{th}}$ shells.

Note 4. The DOS sampling approach

In this note, we discuss the technical details of the density of states (DOS) sampling approach, which is employed to benchmark the accuracy of our Monte Carlo simulations based on the microscopic elastic theory (MET).

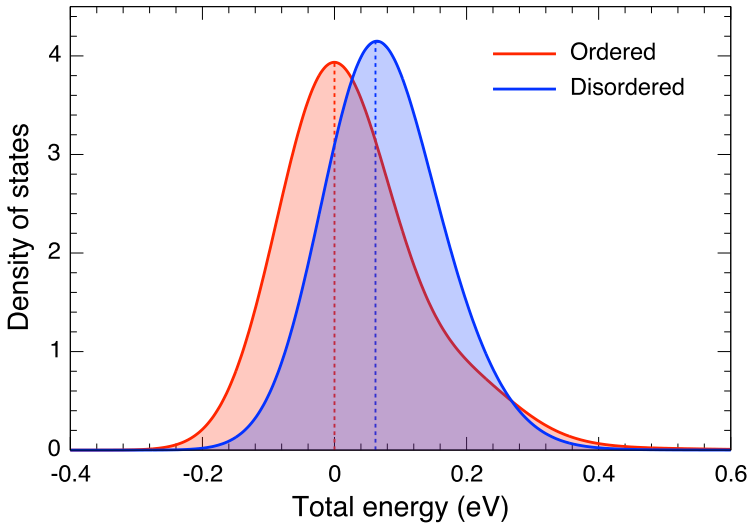

Fig. 4. DOS of the total energies of the ordered and disordered phases obtained from sampling 10^5 configurations for a representative C concentration of 1.2 at.% C.

The internal energy of both the ordered and disordered phases at finite temperature (T) can be computed by

$$\begin{aligned} U =& \frac{\int_{-\infty}^{+\infty} E g(E) \exp(-\frac{E}{k_{\mathrm{B}}T})}{\int_{-\infty}^{+\infty} g(E) \exp(-\frac{E}{k_{\mathrm{B}}T})} \\ =& \frac{\sum_{i=1}^{n} E_i \exp(-\frac{E_i}{k_{\mathrm{B}}T})}{\sum_{i=1}^{n} \exp(-\frac{E_i}{k_{\mathrm{B}}T})}, \end{aligned} \tag{12}$$

where $g(E)$ is the DOS of the energy of the ordered (or disordered) phase. n is the total number of configurations sampled and E_i is the total energy of the i^{th} configuration. k_{B} is the Boltzmann constant.

The DOS of the ordered and disordered phases is randomly sampled using the EAM potential for 10^5 configurations to ensure a full convergence. Each configuration is fully relaxed (shape and atomic positions) using the EAM potential. Figure 4 presents the DOS of the ordered and disordered phases for a representative C concentration, 1.2 at.%. By using Eq. (12), the internal energies of the ordered and disordered phases can thus be computed and are shown in Fig. 5.

The entropy of a system is determined by the number of microscopic states and can thus be expressed by

$$S = k_{\mathrm{B}} \ln \Omega, \tag{13}$$

where Ω is the total number of microscopic configurations.

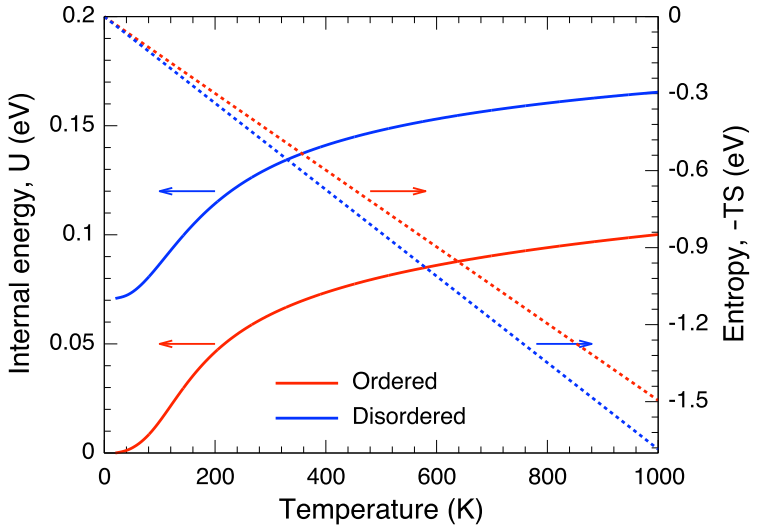

Fig. 5. Internal energies (left y-axis, solid lines) and entropies (right y-axis, dashed lines) of the ordered (red lines) and disordered (blue lines) phases (1.2 at.% C) as a function of temperature.

For the ordered state, its configurational entropy can therefore be derived as

$$\begin{aligned}
S_{\mathrm{ordered}} =& k_{\mathrm{B}} \ln \Omega_{\mathrm{ordered}} \\
=& k_{\mathrm{B}} \ln (C_3^1 \cdot C_{N_{\mathrm{Fe}}}^{N_{\mathrm{C}}}) \\
=& k_{\mathrm{B}} \ln \frac{3 \cdot N_{\mathrm{Fe}}!}{N_{\mathrm{C}}!(N_{\mathrm{Fe}} - N_{\mathrm{C}})!} \\
=& k_{\mathrm{B}} \left[\ln 3 + \ln N_{\mathrm{Fe}}! - \ln N_{\mathrm{C}}! - \ln(N_{\mathrm{Fe}} - N_{\mathrm{C}})!\right] \\
=& k_{\mathrm{B}} \left[\ln 3 + (N_{\mathrm{Fe}} \ln N_{\mathrm{Fe}} - N_{\mathrm{Fe}}) - (N_{\mathrm{C}} \ln N_{\mathrm{C}} - N_{\mathrm{C}})\right. \\
& \left. -((N_{\mathrm{Fe}} - N_{\mathrm{C}}) \ln(N_{\mathrm{Fe}} - N_{\mathrm{C}}) - (N_{\mathrm{Fe}} - N_{\mathrm{C}}))\right] \\
=& k_{\mathrm{B}} \left[\ln 3 + N_{\mathrm{Fe}}(\ln N_{\mathrm{Fe}} - \ln(N_{\mathrm{Fe}} - N_{\mathrm{C}}))\right. \\
& \left. -N_{\mathrm{C}}(\ln(N_{\mathrm{Fe}} - N_{\mathrm{C}}) - \ln N_{\mathrm{C}})\right] \\
=& k_{\mathrm{B}} \left[\ln 3 - N_{\mathrm{Fe}} \ln \frac{N_{\mathrm{Fe}} - N_{\mathrm{C}}}{N_{\mathrm{Fe}}} + N_{\mathrm{C}} \ln \frac{N_{\mathrm{Fe}} - N_{\mathrm{C}}}{N_{\mathrm{C}}}\right],
\end{aligned} \tag{14}$$

where C indicates a combinatorial number. N_{Fe} and N_{C} are the number of Fe and C atoms, respectively.

Similarly, we can derive the configurational entropy for the disordered state as

$$\begin{aligned} S_{\text{disordered}} =& k_{\text{B}} \ln \Omega_{\text{disordered}} \\ =& k_{\text{B}} \ln (C_{N_{\text{Fe}}}^{N_{\text{C}}/3})^3 \\ =& k_{\text{B}} \left[-3N_{\text{Fe}} \ln \frac{3N_{\text{Fe}} - N_{\text{C}}}{3N_{\text{Fe}}} + N_{\text{C}} \ln \frac{3N_{\text{Fe}} - N_{\text{C}}}{N_{\text{C}}} \right]. \end{aligned} \tag{15}$$

Hence, the free energy of the ordered (or disordered) phase can be calculated by

$$F = U - TS. \tag{16}$$

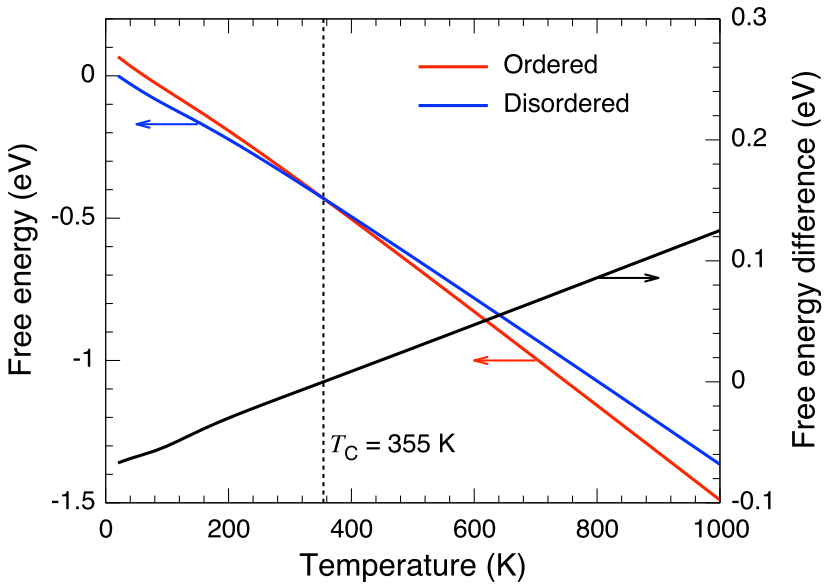

Fig. 6. Free energies (left y-axis) of the ordered (red line) and disordered (blue line) phases (1.2 at.% C), and their difference (right y-axis, black line) as a function of temperature. The black dashed line shows the critical temperature.

The calculated free energies of both the ordered and disordered phases for the C concentration of 1.2 at.% are shown in Fig. 6. By solving the equation $F_{\text{ordered}} = F_{\text{disordered}}$ at different C concentrations, we could then derive the critical temperature as a function of C concentration. In the case shown in Fig. 6, the intersection of the two free-energy curves corresponds to a critical temperature of 355 K.

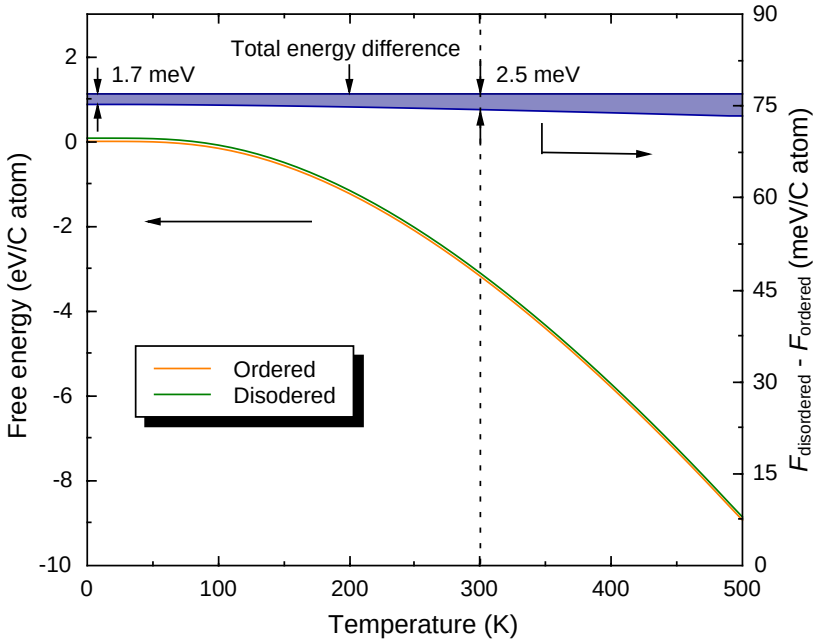

Fig. 7. **Analysis of vibrational free energy.** Helmholtz free energies including lattice vibrations (left y-axis) of two representative configurations (one ordered and one disordered) and their difference (right y-axis) as a function of temperature. As shown by the blue shaded area, the difference in the vibrational free energies of the ordered and disordered configurations is ∼1.7 meV/C atom at $T = 0$ K and ∼2.5 meV/C atom at room temperature, the latter of which is only around 3% of the total energy difference at $T = 0$ K between the two configurations.

Note 5. The self-consistent defect-chemistry (SC) approach

In this approach, we treat the presence of C in bcc Fe as different defects with different formation energies and probabilities of occurrence. Since each C defect interacts with the same tetragonal deformation potential, we introduce the concept of tetragonality dependent formation energies. We consider three types of C defects: monomer (M), single-sublattice dimer (SSD), and double-sublattice dimer (DSD). M denotes a single C atom. SSD refers to a C dimer with two C located on the same sublattice, while DSD denotes the case with two C on different sublattices. The pair interaction energies of different SSDs and DSDs are shown by blue and green circles in Fig. 8a, respectively. For benchmark purposes, we first perform all calculations using the same EAM potential [5] and refine all results using density functional theory (DFT) after validation. As shown in Fig. 8b, we compute the formation energy of each C defect as a function of the tetragonality ($t = c/a$) by

$$E_f^{\parallel}(t) = E_{\text{tot}}^{n\text{Fe}+m\text{C}^{\parallel}}(t) - E_{\text{tot}}^{n\text{Fe}}(t) - m\mu_{\text{C}^{\parallel}}(t), \tag{17}$$

$$E_f^{\perp}(t) = E_{\text{tot}}^{n\text{Fe}+m\text{C}^{\perp}}(t) - E_{\text{tot}}^{n\text{Fe}}(t) - m\mu_{\text{C}^{\perp}}(t), \tag{18}$$

where $E_{\text{tot}}^{n\text{Fe}+m\text{C}^{\parallel}}(t)$ is the total energy of the Fe supercell (n Fe atoms) with m $\text{C}^{\parallel}$ (m = 1 or 2, corresponding to monomer and dimer, respectively) relaxed at a fixed t. Here, $\text{C}^{\parallel}$ ($\text{C}^{\perp}$) indicates that the local distortion direction induced by the C atom is parallel (perpendicular) to the distortion direction of the supercell. We note that since for DSDs two C atoms induce distortions along two different directions, the distortion direction of the supercell can be either parallel to one of them or perpendicular to both. Here, $E_{\text{tot}}^{n\text{Fe}+m\text{C}^{\parallel}}(t)$ refers to the former case, while $E_{\text{tot}}^{n\text{Fe}+m\text{C}^{\perp}}(t)$ denotes the latter. $E_{\text{tot}}^{n\text{Fe}}(t)$ is the total energy of the same body-centered tetragonal (bct) Fe supercell without C. $\mu_{\text{C}^{\parallel}}$ ($\mu_{\text{C}^{\perp}}$) is the chemical potential of $\text{C}^{\parallel}$ ($\text{C}^{\perp}$), which will be determined self-consistently. The formation energies of the $\text{C}^{\parallel}$ defects decrease with increasing the c/a ratio, while those of the $\text{C}^{\perp}$ defects increase (Fig. 8b). This indicates that the $\text{C}^{\parallel}$ defects tend to stabilize the bct Fe-C martensite, while the $\text{C}^{\perp}$ ones destabilize it.

The concentration (x) of a C defect (m C) at temperature (T) follows the Boltzmann distribution.

$$x = m \exp(-\frac{E_f}{k_{\text{B}}T}), \tag{19}$$

where k_{B} is the Boltzmann constant.

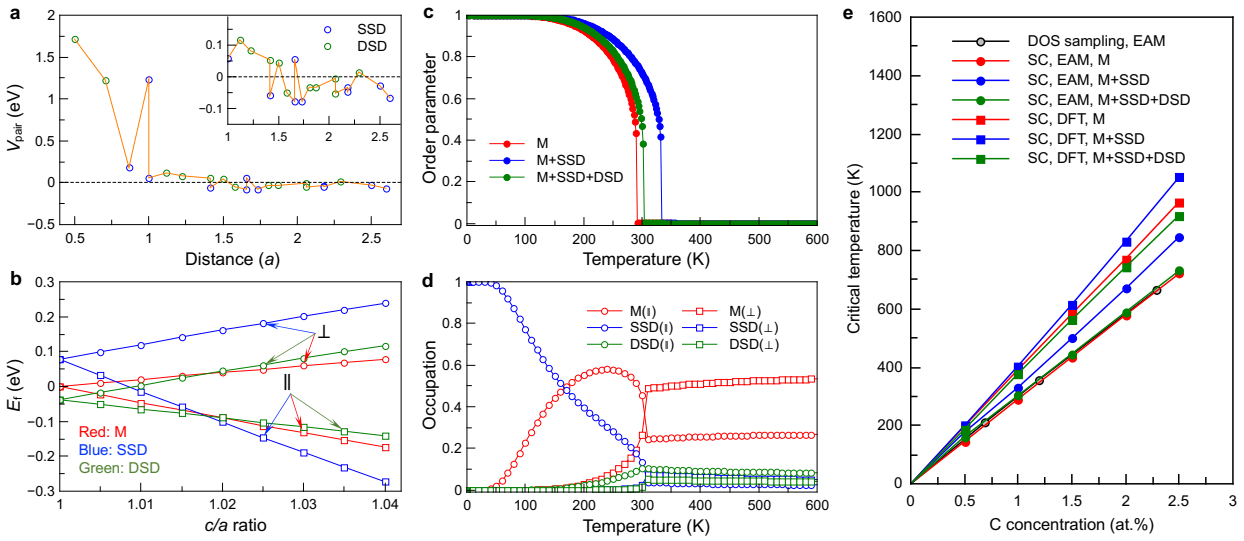

Fig. 8. **a,** Pair interaction energies of C dimers as a function of C-C distance (in units of the lattice constant a) computed from the EAM potential (inset: magnification). **b,** Formation energies of three types of C defects (M, SSD, and DSD) as a function of the c/a ratio when the cell is deformed parallel ($\parallel$) or perpendicular ($\perp$) to the local distortion direction that the C atom induces. Representatively, we show one for each type of C defect. The formation energy of C monomer in bcc Fe is used as the zero energy reference. **c,** Calculated order parameter of the order $\rightarrow$ disorder transition as a function of temperature including different contributions (C concentration: 1 at.%). **d,** Occupation of different defects as a function of temperature. **e,** Simulated critical temperatures as a function of C concentration computed from the SC approach using different inputs (EAM and DFT) compared to the one derived from the DOS sampling approach with the same EAM potential.

The concentration of all types of C interstitial defects should sum up to the total C concentration ($x_{\rm C}$) in the Fe-C alloy. Therefore, the following relation applies.

$$\begin{aligned}(x^{\rm M,\ C^{\parallel}} + 2x^{\rm M,\ C^{\perp}}) + \sum_{i=1}^{N_{\rm SSD}} n_i^{\rm d}(x_i^{\rm SSD,\ C^{\parallel}} + 2x_i^{\rm SSD,\ C^{\perp}}) \\ + \sum_{i=1}^{N_{\rm DSD}} n_i^{\rm d}(2x_i^{\rm DSD,\ C^{\parallel}} + x_i^{\rm DSD,\ C^{\perp}}) = x_{\rm C},\end{aligned} \tag{20}$$

where $N_{\rm SSD}$ ($N_{\rm DSD}$) is the total number of SSD (DSD) defects considered and $n_i^{\rm d}$ is the degeneracy factor of the $i^{\rm th}$ defect. For given t, T and $x_{\rm C}$, one can thus solve Eq. (20) to obtain the chemical potential of C, $\mu_{\rm C}(t)$.

Once $\mu_C(t)$ is determined, all x_i can be computed, based on which the fraction of C atoms occupying octahedral sublattice i (o_i , $i = 1, 2, 3$) can be calculated. Thus, the order parameter θ can be evaluated following the definition given in Ref. [6] as given by Eqs. (9) and (10) in the paper.

Then, the tetragonality t can be updated by

$$t^{\text{updated}} = 1 + \gamma x_C \theta, \tag{21}$$

where γ describes the linear dependence of t of the fully ordered phase on C concentration, which can be computed from EAM potentials or DFT (see Table 1). Since t is definite, t^{updated} should be consistent with t. Moreover, with the updated t, we can compute μ_C again using Eq. (20). By using Eq. (21), t can then be updated again. Therefore, t can be computed in a self-consistent manner.

TABLE 1. Comparison of lattice constant, elastic constants of bcc Fe and the γ parameter obtained from EAM, DFT and experiments [7–9].

Method	a (Å)	c_{11} (GPa)	c_{12} (GPa)	c_{44} (GPa)	γ (1/at.%)
EAM	2.867	243	138	122	0.01030
DFT	2.834	277	140	92	0.01026
Experiment	2.867	243	138	122	0.01025

In this way, the tetragonality (t), the order parameter (θ), the C chemical potential (μ_C) and the occupation of different defects can all be determined as a function of temperature and C concentration self-consistently. The order parameter for a representative case of 1 at.% C is shown in Fig. 8c. At low temperatures, the system favors the ordered state and undergoes a phase transition to the disordered state with increasing temperature. The critical temperature is ∼303 K. Using the SC approach, we can also easily separate the contributions from monomers and dimers. As shown in Fig. 8c, the major contribution is from the monomers. The SSDs enhance the critical temperature by ∼40 K, while the DSDs decrease the critical temperature by ∼28 K. This clearly demonstrates that the ordered Fe-C martensite is mainly stabilized by monomers rather than dimers. The C dimers indeed impact the critical temperature, but due to counteraction of the SSDs and DSDs, the dimers

have a limited effect on the critical temperature (see Fig. 8e).

The SC approach also yields the occupation of different defects at finite temperatures (Fig. 8d). At low temperatures the system favors the SSDs with $C^{\parallel}$ and forms a fully ordered phase. When temperature increases, the system starts forming $C^{\parallel}$ monomers. Close to the critical temperature, there is a sharp increase of $C^{\perp}$ monomers and a remarkable decrease in SSDs and $C^{\parallel}$ monomers. This significantly decreases the order parameter and triggers the order $\rightarrow$ disorder transition. At high temperatures, the system mostly consists of monomers (both $C^{\parallel}$ and $C^{\perp}$) because of configurational entropy, leading to a fully disordered state.

Figure 8e shows the critical temperatures from our SC approach using both EAM and DFT inputs compared to the DOS sampling result using the same potential (see Note 4). It can be seen that the two approaches show good agreement, which validates our SC approach. Qualitatively, the DFT-based results are similar to the EAM ones, but quantitatively DFT gives slightly higher critical temperatures.

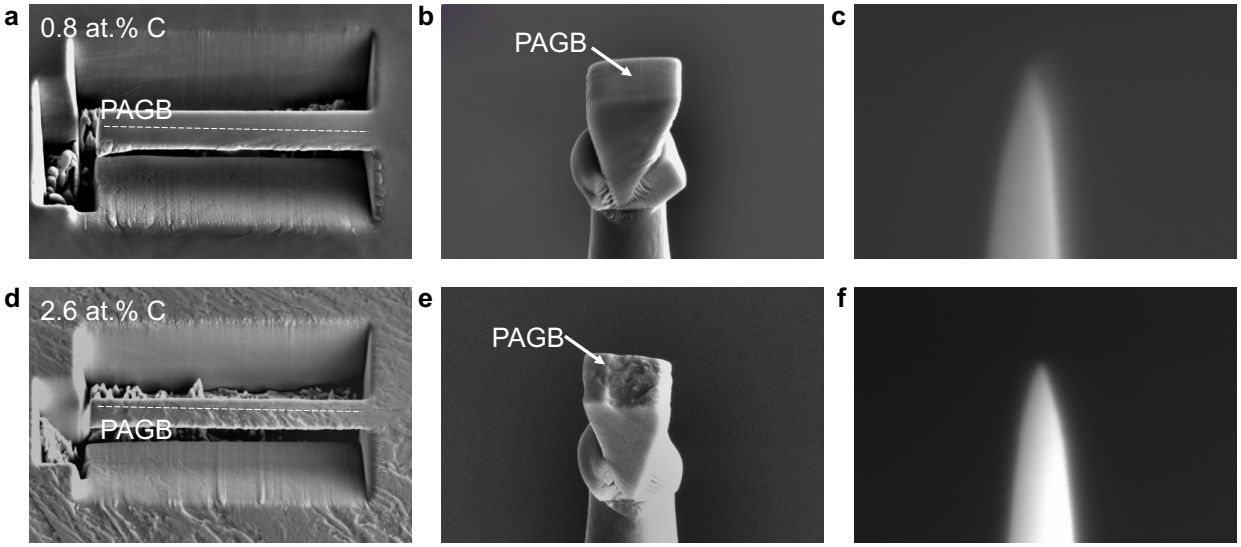

Fig. 9. **Preparation of specimens containing a prior-austenite grain boundary (PAGB). a**, A wedge containing a grain boundary is cut loose from the bulk for the sample with 0.8 at.% C. **b**, A part of the wedge being transferred to a Si-post. **c**, Careful annular milling performed to slowly remove material, creating a tip with the grain boundary. **d-e**, Same preparation procedure for a different sample with 2.6 at.% C.

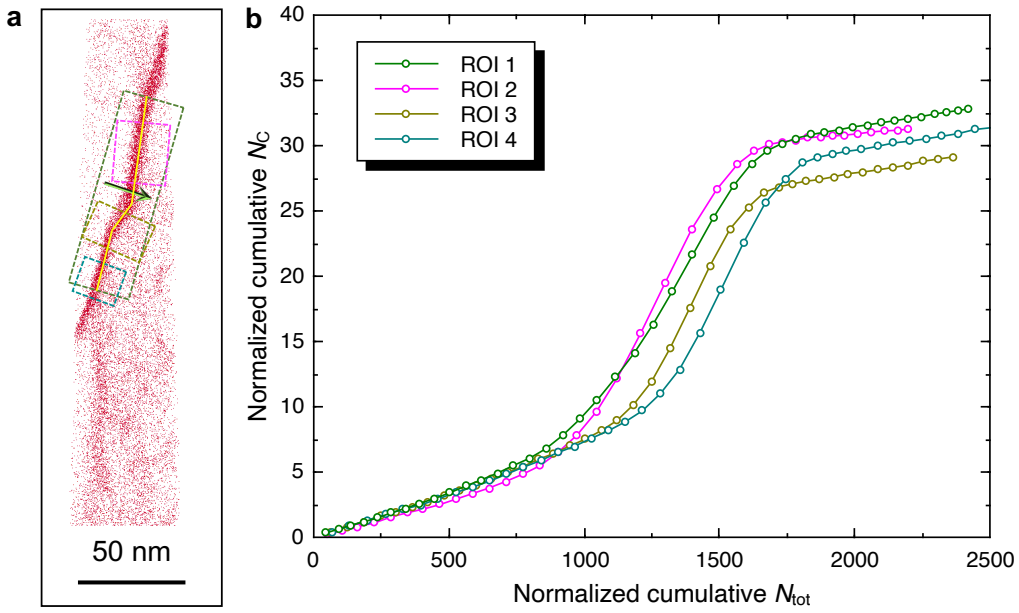

Fig. 10. **Analysis of grain boundary roughness.** **a**, Selection of four regions of interest (ROI) on the atom probe tomography (APT) tip for the sample with 0.8 at.% C as highlighted by the colored rectangles across the grain boundary. The yellow line tracks the direction of the grain boundary and divides the rough interface into three segments of flat interfaces. By comparing the total length of the "zig-zag" grain boundary to that of the one approximated as flat (i.e., the length of the green rectangle), we estimate the increase in the interface area due to roughness, which is ∼2% relative to the flat grain boundary. **b**, Quantitative analysis of the Gibbsian interfacial excess of C for the four ROI in panel **a**. The colors of the lines in panel **b** correspond to the colors of rectangles of the selected ROI in panel **a**. N_C and N_{tot} are the cumulative number of C and of all atoms, respectively, normalized by the selected grain boundary areas. The Gibbsian interfacial excess of C (Γ) taking into account the grain boundary roughness is 20±2 at./nm^2.

[1] Krivoglaz, M. A. *X-Ray and Neutron Diffraction in Nonideal Crystals* (Springer-Verlag, Berlin, 1996).

[2] Khachaturyan, A. G. *Theory of Structural Transformations in Solids* (Wiley, New York, 1983).

[3] Klotz, S. & Braden, M. Phonon dispersion of bcc iron to 10 GPa. *Phys. Rev. Lett.* **85**, 3209–3212 (2000).

[4] Kong, L. T. Phonon dispersion measured directly from molecular dynamics simulations. *Comput. Phys. Commun.* **182**, 2201–2207 (2011).

[5] Lau, T. T., Först, C. J., Lin, X., Gale, J. D., Yip, S., & Van Vliet, K. J. Many-body potential for point defect clusters in Fe-C alloys. *Phys. Rev. Lett.* **98**, 215501 (2007).

[6] Uebing, C. On the ordering of interstitials in bcc metals and bct martensites: A lattice gas approach. *Scr. Metall. Mater.* **30**, 1183–1188 (1994).

[7] Kurdjumov, G. V. & Khachaturyan, A. G. Phenomena of carbon atom redistribution in martensite. *Metall. Trans.* **3**, 1069–1076 (1972).

[8] Roberts, C. S. Effect of carbon on the volume fractions and lattice parameters of retained austenite and martensite. *Trans. AIME* **197**, 203–204 (1953).

[9] Rayne, J. A. & Chandrasekhar, B. S. Elastic constants of iron from 4.2 to 300 K. *Phys. Rev.* **122**, 1714 (1961).